CALCULATION OF REALISTIC CHARGED-PARTICLE TRANSFER MAPS*

C E. Mitchell and A. J. Dragt, University of Maryland, USA

Abstract

The stability of orbits in storage and damping rings can depend sensitively on nonlinear fringe-field and high-order-multipole effects in the various beam-line elements. The inclusion of these effects requires a detailed and realistic model of the interior and fringe electric and magnetic fields, including their high spatial derivatives. In the case of magnetic elements a collection of surface fitting methods has been developed for extracting this information accurately from 3-dimensional magnetic field data on a grid, as provided by various 3-dimensional finite element field codes. The virtue of surface methods is that they exactly satisfy the Maxwell equations and are relatively insensitive to numerical noise in the data. These techniques can be used both to compute realistic design orbits and realistic high-order transfer maps about these orbits. An exactly soluble but numerically challenging model field is used to provide a rigorous collection of performance benchmarks.

BACKGROUND

For the design of high-performance storage or damping rings it is essential to have realistic electric and magnetic field information for the various beam-line elements, in order to compute accurate design orbits and high-order transfer maps about the design orbits. Realistic field data can be provided on a grid with the aid of various 3-dimensional finite element codes, sometimes spot checked against measured data. But the computation of high-order transfer maps based on this data appears to pose an insurmountable problem: the calculation of high-order transfer maps requires a knowledge of high derivatives of the field data. The direct calculation of high derivatives based only on grid data is intolerably sensitive to noise (due to truncation or round-off) in the grid data. We will see that this problem can be overcome by the use of surface methods. The effect of numerical noise can be overcome by fitting onto a bounding surface far from the beam axis and continuing inward using the Maxwell equations. While the process of differentiation serves to amplify the effect of numerical noise, the process of continuing inward using the Maxwell equations is *smoothing*. This smoothing is related to the fact that harmonic functions take their extrema on boundaries. When using surface methods, all fits are made to such boundaries. Therefore if these fits are accurate, interior data based on these fits will be even more accurate.

In this paper we will devote our attention to magnetic beam-line elements. (For a treatment of RF cavities, see [1].) Two cases have been treated separately: straight and curved. For straight beam-line elements such as quadrupoles, sextupoles, octupoles, and wiggglers, it is convenient to employ cylindrical surfaces. These surfaces may have circular, elliptical, or rectangular cross sections. We will describe the use of elliptical cylinders. The use of circular and rectangular cylinders is described elsewhere [2, 3, 4]. For the case of curved magnetic elements such as dipoles with large design-orbit sagitta, we will employ the surface of a bent box with straight ends. In all cases the bounding surface will surround the design orbit within the beam-line element and will extend into the fringe-field regions outside the beam-line element, thus taking into account all fringe-field effects as well as all effects within the body of the beam-line element.

For the case of straight beam-line elements it is convenient to describe the magnetic field in terms of a magnetic scalar potential ψ. Then, if one wishes to compute transfer maps in terms of canonical coordinates, one can proceed with the aid of an associated vector potential $\boldsymbol{A}$ computed from ψ. Alternatively, if one wishes to integrate noncanonical equations employing the magnetic field $\boldsymbol{B}$, it can be obtained from the relation $\boldsymbol{B} = \nabla\psi$.

For the case of curved beam-line elements it is convenient to work directly with the vector potential. Its use in the case of canonical coordinates is then immediate. If instead one wishes to integrate noncanonical equations employing the magnetic field $\boldsymbol{B}$, it can be obtained from the relation $\boldsymbol{B} = \nabla \times \boldsymbol{A}$.

In this paper we will first treat the case of straight beam-line elements. For this case a cylindrical multipole expansion for ψ is convenient. In Sections II-III we will describe such an expansion and how it can be computed based on $\boldsymbol{B}$ data provided on a grid and interpolated onto the surface of an elliptical cylinder. In Section IV we will treat the case of curved beam-line elements. In this case $\boldsymbol{A}$ will be computed based on both $\boldsymbol{B}$ and ψ data provided on a grid and interpolated onto the surface of a bent box.

CYLINDRICAL HARMONIC EXPANSIONS

In a current-free region the magnetic field $\boldsymbol{B}$ is curl free, and can therefore can be described in terms of a magnetic scalar potential. Because $\boldsymbol{B}$ is also divergence free, ψ must obey the Laplace equation $\nabla^2\psi = 0$. A general solution ψ satisfying the Laplace equation in cylindrical coordinates

* Work supported by U.S. Department of Energy Grant DE-FG02-96ER40949.

and analytic near the axis $\rho = 0$ takes the form

$$\psi(\rho,\phi,z) = \sum_{m=0}^{\infty} \int_{-\infty}^{\infty} dk\; I_m(k\rho) e^{ikz} \left[G_{m,s}(k)\sin m\phi + G_{m,c}(k)\cos m\phi\right]. \quad (1)$$

By utilizing the Taylor series of the modified Bessel function I_m we may write ψ in the form of a cylindrical harmonic (multipole) expansion:

$$\psi(\rho,\phi,z) = \sum_{m=0}^{\infty} \left[\psi_{m,s}(\rho,z)\sin m\phi + \psi_{m,c}(\rho,z)\cos m\phi\right], \quad (2)$$

where for $\alpha = s, c$,

$$\psi_{m,\alpha}(\rho,z) = \sum_{l=0}^{\infty} \frac{(-1)^l m!}{2^{2l} l!(l+m)!} C^{[2l]}_{m,\alpha}(z)\rho^{2l+m}. \quad (3)$$

The functions $C^{[n]}_{m,\alpha}$, known as generalized gradients, are defined by

$$C^{[n]}_{m,\alpha}(z) = \frac{i^n}{2^m m!} \int_{-\infty}^{\infty} dk\; e^{ikz} k^{m+n} G_{m,s}(k). \quad (4)$$

Once they are known, ψ is specified. Note that $C^{[n]}_{m,\alpha}(z) = d^n C^{[0]}_{m,\alpha}(z)/dz^n$.

FITTING USING AN ELLIPTICAL CYLINDER

We will now describe how the generalized gradients can be computed based on $\boldsymbol{B}$ data provided on a grid and interpolated onto the surface of an elliptical cylinder. Elliptic coordinates in the x, y plane are described by the relations

$$x = f\cosh(u)\cos(v),\;\; y = f\sinh(u)\sin(v). \quad (5)$$

Contours of constant u, with $u \in [0,\infty]$, are nested ellipses with common foci located at $(x;y) = (\pm f;0)$. Contours of constant v, with $v \in [0, 2\pi]$, are hyperbolae. Together these contours form an orthogonal coordinate system.

Suppose we are provided with the three components of the magnetic field on a regular 3-d Cartesian grid. Consider an elliptical cylinder surrounding the axis of the magnetic element, which lies within all iron and other magnetic sources. Such a surface is obtained by setting $u = U$ and allowing the coordinates v, z to vary. This data can then be interpolated onto the surface of the elliptical cylinder to obtain the normal component B_u of the field on this surface.

Define the functions F_ℓ and G_ℓ in terms of the surface data as

$$F_\ell(U,k) = \int_{-\pi}^{\pi} \sqrt{J(U,v)}\tilde{B}_u(U,v,k) se_\ell(v,q)dv, \quad (6a)$$

$$G_\ell(U,k) = \int_{-\pi}^{\pi} \sqrt{J(U,v)}\tilde{B}_u(U,v,k) ce_\ell(v,q)dv. \quad (6b)$$

Here $\tilde{B}_u(U,v,k)$ is the Fourier transform of $B_u(U,v,z)$, se_ℓ and ce_ℓ are Mathieu functions [5, 6], $J(u,v)$ is the Jacobian of the mapping from Cartesian to elliptic coordinates, and $q = -k^2 f^2/4$. The on-axis gradients are now given by

$$C^{[n]}_{m,\alpha}(z) = \frac{i^n}{2^m m!}\frac{1}{\sqrt{2\pi}} \int_{-\infty}^{\infty} k^{m+n} e^{ikz} \beta^{\alpha}_m(U,k)dk \quad (7)$$

where

$$\beta^s_m(U,k) = \sum_{\ell=0}^{\infty} g^\ell_s(k) E^{(\ell)}_m(k) \left[\frac{F_\ell(U,k)}{Se'_\ell(U,q)}\right], \quad (8a)$$

$$\beta^c_m(U,k) = \sum_{\ell=0}^{\infty} g^\ell_c(k) D^{(\ell)}_m(k) \left[\frac{G_\ell(U,k)}{Ce'_\ell(U,q)}\right]. \quad (8b)$$

Here Se_ℓ and Ce_ℓ are modified Mathieu functions, and g^ℓ_α, $D^{(\ell)}_m$, $E^{(\ell)}_m$ are known functions that relate Mathieu and Bessel functions [3, 4].

Benchmarks

Here we describe an exactly-soluble but numerically challenging model field to be used to numerically benchmark the procedure just described. Suppose two magnetic monopoles having strengths $\pm g$ are placed at the (x,y,z) locations

$$r^+ = (0,a,0),\; r^- = (0,-a,0). \quad (9)$$

These monopoles generate a scalar potential $\psi(x,y,z)$ given by the relation

$$\psi(x,y,z) = \psi_+(x,y,z) + \psi_-(x,y,z) = -g[x^2+(y-a)^2+z^2]^{-1/2} + g[x^2+(y+a)^2+z^2]^{-1/2}. \quad (10)$$

Due to the symmetries of the field, it can be shown that the only nonvanishing associated generalized gradients $C^{[n]}_{m,\alpha}$ are those with $\alpha = s$ and m odd. They have the values

$$C^{[0]}_{m,s}(z) = (-1)^{(m-1)/2}\frac{g}{a^{m+1}}\frac{(2m)!}{2^{2m-2}(m!)^2}\beta^{2m+1}(z) \quad (11a)$$

where

$$\beta(z) = \frac{a}{\sqrt{z^2+a^2}}. \quad (11b)$$

This result has been used to benchmark the technique described in the previous section in the case that $a = 2.4$ cm and $g = 1$ Tesla-$(\mathrm{cm})^2$. We set up a regular grid in x, y, z space, where we let each variable range over the intervals $x \in [-4.4, 4.4]$ with spacing $h_x = 0.1$, $y \in [-2.4, 2.4]$ with $h_y = 0.1$, and $z \in [-300, 300]$ with $h_z = 0.125$ (in units of cm). The values of the magnetic field at each grid point are computed using $\boldsymbol{B} = \nabla\psi$.

Consider an elliptical cylinder of semimajor axis $x_{max} = 4$ cm, semiminor axis $y_{max} = 2$ cm, and length 600 cm. We use bicubic interpolation to interpolate $\mathbf{B}$ at

these grid points onto 120 selected angular points on the cylinder, for each of the 4801 selected values of z. The angular integration in (6) is performed using a Riemann sum with $N = 120$. (This is necessary to ensure sufficient convergence of the angular integrals to within 10^{-4}.) We evaluate the Fourier transform at 401 values of k in the range $[-K_c, K_c]$ with $K_c = 20$, using a spline-based Fourier transform algorithm. We use these same points in k space to evaluate the inverse Fourier transform, providing a set of numerically determined functions $C^{[n]}_{m,\alpha}(z)$.

Suppose, for example, we wish to obtain the transfer map for the monopole doublet through terms of degree 7. We then require the generalized gradient functions $C^{[n]}_{m,s}(z)$ with $(m+n) \leq 7$. For each of these functions, we find that the relative difference between the numerical results and (11) is on the order of 10^{-4} or smaller.

Smoothing

The key feature of this technique is that results are relatively insensitive to surface errors due to smoothing. That is, each kernel multiplying the surface functions F_ℓ and G_ℓ in (8) falls off rapidly with spatial frequency k. As a result, high frequency noise appearing in the boundary data has little effect on the functions $C^{[n]}_{m,\alpha}$ of (7).

To illustrate this effect, let $B_y(0,0,z)$ denote the on-axis monopole doublet field and make the noise model

$$B_x^{noise}(x_j, y_j, z_j) = \epsilon B_y(0,0,z_j)\delta_x(j), \qquad (12)$$

$$B_y^{noise}(x_j, y_j, z_j) = \epsilon B_y(0,0,z_j)\delta_y(j), \qquad (13)$$

where $\delta_x(j)$ and $\delta_y(j)$ are uniformly distributed random variables taking values in the interval $[-1, 1]$. We take $\epsilon = 0.01$, obtaining a random distribution of field values that are proportional at the 1% level to the on-axis vertical field of the monopole doublet. Figs. 1-2 illustrate the generalized gradients $C^{[0]}_{7,c}$ and $C^{[6]}_{1,c}$ as computed from these values using (7). The solid line illustrates the rms value of the generalized gradient at each value of z, as computed using a circular cylinder of radius $R = 2$ cm. The dashed line illustrates the rms value of the generalized gradient at each value of z as computed using a circumscribed elliptical cylinder of semiminor axis 2 cm and semimajor axis 4 cm. In each case we find that a 1% noise in the surface data produces only a 0.01% error or less in the generalized gradients. These figures also illustrate that fitting to the surface of an elliptical cylinder leads to greater suppression of noise than fitting to an inscribed circular cylinder. This is consistent with what we expect if errors in the surface data are suppressed with increasing distance from the bounding surface. We see that it is advantageous to use a fitting surface which is as far from the axis as possible.

Applications

A less stringent test of the accuracy of this procedure (but also a test of the quality of the magnetic data on the mesh) is that the magnetic field computed from the surface data should reproduce the magnetic field at the interior grid points. We computed such an interior fit for the modified CESR-c design of the Cornell wiggler, which has been adopted as the design prototype for use in International Linear Collider studies. Cornell provided data obtained from the 3-dimensional finite element modeling code OPERA-3d for the field components B_x, B_y, and B_z on a grid of spacing $0.4 \times 0.2 \times 0.2$ cm in a volume $10.4 \times 5.2 \times 480$ cm, extending beyond the fringe-field region. An elliptic cylinder with semimajor axis 4.4 cm and semiminor axis 2.4 cm was placed in the domain of the data, and the field on the elliptic cylinder boundary was constructed using nearest-neighbor interpolation with cubic splines. See Fig. 3.

The interior field was computed using generalized gradients through terms of degree 6 in x, y over the domain

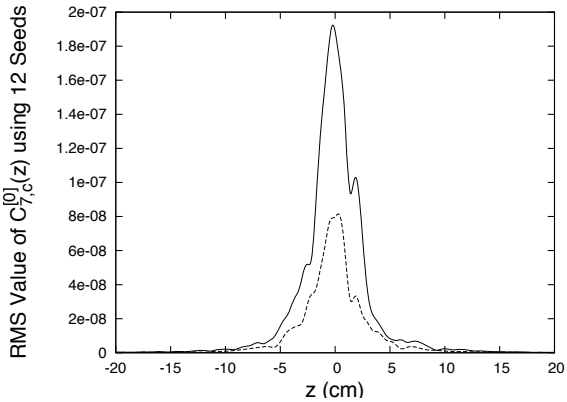

Figure 1: The quantity $C^{[0]}_{7,c}(z)$ computed from a field consisting of random noise. (Solid line) Values computed using a circular cylinder of radius $R = 2$ cm. (Dashed line) Values computed using an elliptical cylinder of semimajor axis $x_{max} = 4$ cm and semiminor axis $y_{max} = 2$ cm.

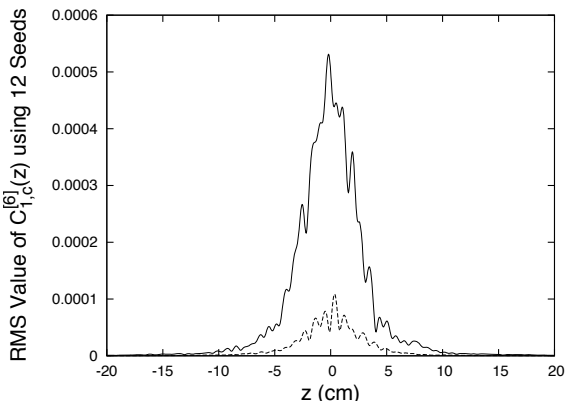

Figure 2: The quantity $C^{[6]}_{1,c}(z)$ computed from a field consisting of random noise. (Solid line) Values computed using a circular cylinder of radius $R = 2$ cm. (Dashed line) Values computed using an elliptical cylinder of semimajor axis $x_{max} = 4$ cm and semiminor axis $y_{max} = 2$ cm.

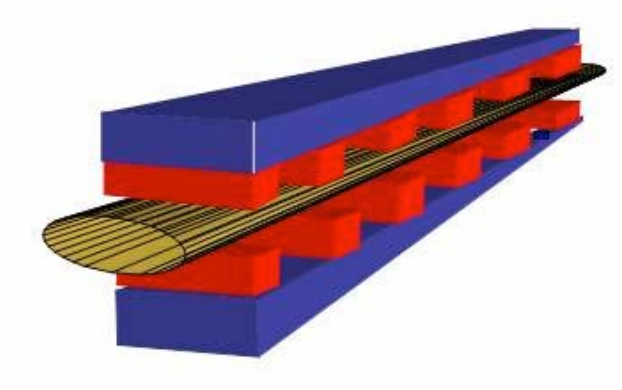

Figure 3: Schematic of the ILC wiggler and an elliptic cylinder centered on the z-axis, fitting within the bore of the wiggler, and extending beyond the fringe-field regions at the ends of the wiggler.

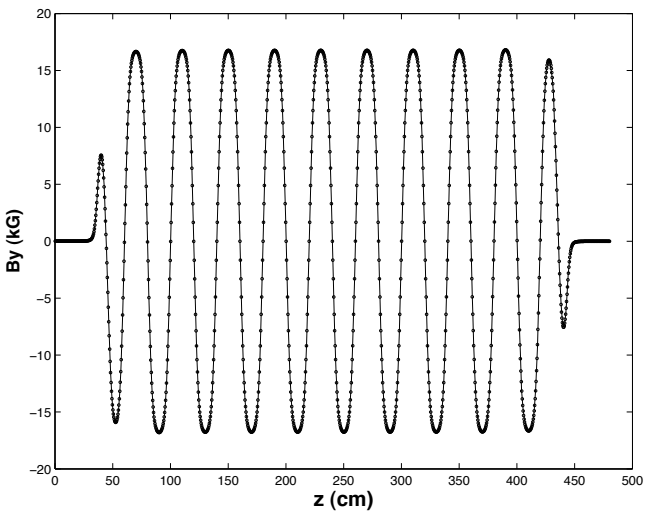

Figure 4: Fit obtained to proposed ILC wiggler vertical field using the elliptic cylinder of Fig. 3. The solid line is computed from surface data; dots are numerical data provided by OPERA-3d.

of the original data. This solution for the interior field was then compared to the original data at each grid point. Fig. 4 displays the fit to the vertical field B_y off-axis at $(x, y) = (0.4, 0.2)$ cm along the length of the wiggler. Note that the fitted field captures the fringe-field behavior. The RMS error obtained was $|\mathbf{B}_{data} - \mathbf{B}_{fit}|/|\mathbf{B}|_{peak} = 3.5 \times 10^{-4}$. All other field components are fit equally well at all interior points.

FITTING USING A BENT BOX

In this section we consider magnetic elements with large sagitta. We employ a bent box with straight ends surrounding the region of the beam, but excluding all iron or other sources (Fig. 5). Suppose $\mathbf{B}$ and ψ are given on a grid, and these data are then interpolated onto the boundary of the box, which we call Γ. Given such values on Γ, the vector potential is given as the sum of two terms, $\mathbf{A} = \mathbf{A}^n + \mathbf{A}^t$, where

$$\mathbf{A}^n(\mathbf{r}) = \int_\Gamma [\mathbf{n}(\mathbf{r}') \cdot \mathbf{B}(\mathbf{r}')]\mathbf{G}^n(\mathbf{r}; \mathbf{r}', \mathbf{m}(\mathbf{r}'))dS',$$
$$\mathbf{A}^t(\mathbf{r}) = \int_\Gamma \psi(\mathbf{r}')\mathbf{G}^t(\mathbf{r}; \mathbf{r}', \mathbf{n}(\mathbf{r}'))dS'. \quad (14)$$

Here $\mathbf{n}(\mathbf{r}')$ denotes the unit normal and $\mathbf{m}(\mathbf{r}') = \mathbf{r}'/r'$ at each point $\mathbf{r}'$ on the surface of the box. The vector-valued integration kernels $\mathbf{G}^n$ and $\mathbf{G}^t$ are given by [3, 7]

$$\mathbf{G}^n(\mathbf{r}; \mathbf{r}', \mathbf{m}(\mathbf{r}')) = \frac{\mathbf{m} \times (\mathbf{r} - \mathbf{r}')}{4\pi|\mathbf{r} - \mathbf{r}'|(|\mathbf{r} - \mathbf{r}'| - \mathbf{m} \cdot (\mathbf{r} - \mathbf{r}'))},$$
$$\mathbf{G}^t(\mathbf{r}; \mathbf{r}', \mathbf{n}(\mathbf{r}')) = \frac{\mathbf{n}(\mathbf{r}') \times (\mathbf{r} - \mathbf{r}')}{4\pi|\mathbf{r} - \mathbf{r}'|^3}. \quad (15)$$

It can be verified that each kernel $\mathbf{G}^\alpha$ has the two properies $\nabla \cdot \mathbf{G}^\alpha = 0$ and $\nabla \times \nabla \times \mathbf{G}^\alpha = 0$ within the region of interest, where derivatives are taken with respect to the variable $\mathbf{r}$. As a result, the vector potential $\mathbf{A}$ given by (14) shares these properties. It follows that $\nabla \cdot \mathbf{B} = 0$ and $\nabla \times \mathbf{B} = 0$, and $\mathbf{A}$ satisfies the Coulomb gauge condition, for any surface data $\mathbf{n} \cdot \mathbf{B}$ and ψ, even if the data are noisy and the surface integrals are only evaluated approximately. Furthermore, $\mathbf{G}^n$ and $\mathbf{G}^t$ are analytic within the region of interest, and therefore $\mathbf{A}$ is also analytic in this region. By expanding the kernels $\mathbf{G}^\alpha$ as power series in the transverse variables x and y, we may obtain corresponding power series for the vector potential $\mathbf{A}$.

This method has been implemented in a Fortran 90 routine [3]. This routine uses efficient truncated power series algebra (TPSA) algorithms to compute the Taylor series of the integral kernels (15) about each point on the design orbit. Each Taylor coefficient of the vector potential $\mathbf{A}$ at a fixed value of z requires a single integration of the field and potential data over the surface Γ. The resulting coefficients may then be utilized to find design orbits and high-order transfer maps about these orbits.

Benchmarks

Consider the monopole doublet field described earlier. We interpolate $\mathbf{B}$ and ψ onto the surface of a bent box with a bending angle of 30 degrees, and then employ the method described in the previous section to compute the vector potential $\mathbf{A}$ and its Taylor coefficients about each point along a path through the center of the box using (14). See Fig. 5. The resulting vector potential is shown in Fig. 6 as a function of path length through the center of the box.

Using the power series for $\mathbf{A}$, power series for the components of $\mathbf{B}$ about each reference point $\mathbf{r}_d$ are computed using $\mathbf{B} = \nabla \times \mathbf{A}$. These results can then be compared to the known Taylor coefficients of the field. We find that all computed coefficients through terms of degree 4 are accurate to 10^{-6} in the arc section of the box, in the region

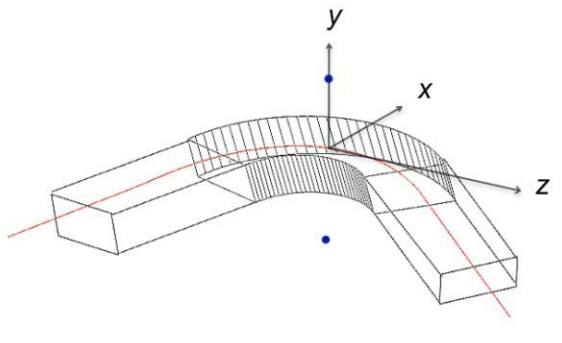

Figure 5: Illustration of a monopole doublet and a bent box with straight ends. The two dots denote equal and opposite magnetic charges. The red curve denotes a path through the center of the box.

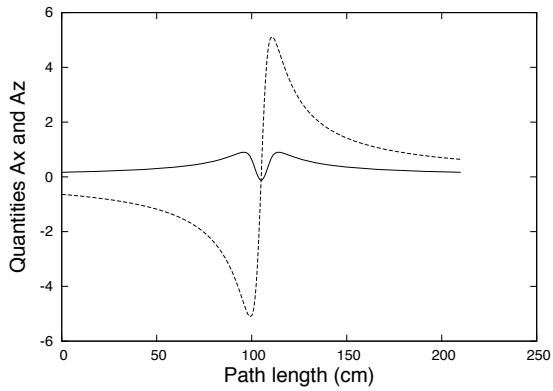

Figure 6: The vector potential of the monopole doublet illustrated in Fig. 5, computed from surface data, along a curved trajectory through the center of the bent box. In this case $A_y = 0$ and the quantities A_x (dashed line) and A_z (solid line) are plotted versus path length.

where the field is rapidly varying. This error increases very near the ends of the straight sections to 10^{-4}. The error at the ends is due to the fact that the field of a monopole doublet falls off quite slowly. The error would have been smaller had the straight ends of the box been made longer. The smoothing of numerical noise, as described earlier, can also be shown to occur in the case of the bent box. A detailed discussion of this issue can be found in [3].

CONCLUSIONS

A collection of surface fitting methods has been developed for providing accurate interior field data in analytic form based on 3-dimensional magnetic field data on a grid, as provided by various 3-dimensional finite element field codes. Each of these methods involves fitting field data onto a boundary surface and continuing inward to obtain ψ and/or $\mathbf{A}$ and their Taylor coefficients in a neighborhood of the beam. These surface-fitting procedures have several distinct advantages:

- The Maxwell equations are exactly satisfied.
- The results are manifestly analytic in all variables.
- The error is globally controlled. Both the exact and computed fields satisfy the Laplace equation. Therefore their difference, the error field, also satisfies the Laplace equation, and must take its extrema on the boundary. The fitting error on the boundary is controlled, and the interior error must therefore be even smaller.
- Interior values inferred from surface data are relatively insensitive to errors/noise in the surface data. In general, the sensitivity to noise in the data decreases rapidly (as some high inverse power of distance) with increasing distance from the surface, and this property improves the accuracy of the high-order interior derivatives needed to compute high-order transfer maps.

As a result one can, for the first time, obtain a realistic high-order transfer map for an entire accelerator or storage ring without the uncertainties associated with the use of only approximate field models.

REFERENCES

[1] D. Abell, "Computation of High Order Maps for RF Cavities from Surface Data," these proceedings.

[2] M. Venturini and A. Dragt, Nucl. Inst. and Meth. A 427, 387 (1999).

[3] C. Mitchell, "Calculation of Realistic Charged-Particle Transfer Maps," Ph. D. thesis, University of Maryland, College Park (2007), `http://www.physics.umd.edu/dsat/`.

[4] A. Dragt, *Lie Methods for Nonlinear Dynamics with Applications to Accelerator Physics*, University of Maryland Technical Report (2009), `http://www.physics.umd.edu/dsat/`.

[5] M. Abramowitz and I. Stegun, *Handbook of Mathematical Formulas and Integrals* (Academic Press, 1995).

[6] N. McLachlan, *Theory and Application of Mathieu Functions* (Dover Publications, Inc., 1964).

[7] A. Dragt, T. Stasvevich, and P. Walstrom, "Computation of charged-particle transfer maps for general fields and geometries using electromagnetic boundary-value data," PAC'01, Chicago, IL, June 2001, p. 1776 (2001).